Earth and Planetary Science Letters

New insights into rift evolution from data-constrained burial and thermal histories at the northern South China Sea margin

--Manuscript Draft--

Manuscript Number:	
Article Type:	Letters
Keywords:	South China Sea northern margin; rifted margin thermal evolution; vitrinite reflectance; biomarkers; thermal modelling
Corresponding Author:	Andrea Schito, PhD University of Barcelona Barcelona, Catalunya SPAIN
First Author:	Andrea Schito, PhD
Order of Authors:	Andrea Schito, PhD
	Geoffroy Mohn, PhD
	Zhibin Wen, PhD
	Sveva Corrado, Professor
	Michael Nirrengarten, PhD
	Laura Gutiérrez-García
	Stephen Bowden, PhD
Abstract:	The evolution of the rifted margin of the northern South China Sea challenges predictions of previous models but a knowledge gap still exists regarding how thermal history varies at different locations and times of rifting. International Ocean Discovery Program (IODP) Expeditions 367/368/368X collected samples of sediment that can be used to model the thermal evolution at different rifting stages in the distal margin and oceanic crust. Modelling results outline a thermal history driven by the interplay of different tectonic processes that are sometimes at odds with the main theoretical models. The most proximal location has a burial history that includes the unroofing of ~3km of sediment before the increase of heat flow during rifting and break up prior to cooling to the present day. In the more distal part, short, localised peaks in heat flow due to syn-rift magmatism are recorded while, the oceanic crust has a thermal regime decoupled from that of the continental section and here the rate of cooling abruptly decreased in final post-rift phases. Thus, while the transect drilled in IODP 367/368 may represent a transition from continental to ocean crust, the thermal regimens sampled by are not end-members in a simple continuum and instead capture fundamental steps in the thermal evolution of the distal rifted margin of the northern South China Sea. On a global scale, this dataset represents one of the most complete samplings of a distal rifted margin providing critical new constrains on the thermal evolution during formation of rifted margins.

New insights into rift evolution from data-constrained burial and thermal histories at the northern South China Sea margin

Andrea Schito[1,2,3], Geoffroy Mohn[4], Zhibin Wen [2], Sveva Corrado[5], Michael Nirrengarten[4], Laura Gutiérrez-García[4], Stephen Bowden[2]*

[1] Department of Mineralogy, Petrology and Applied Geology, Facultat de Ciències de la Terra, Universitat de Barcelona, Carrer Martí i Franquès s/n, 08028, Barcelona, Spain

[2] Department of Geology and Petroleum Geology, University of Aberdeen, Aberdeen AB24 3UE, UK

[3] Institut de Recerca Geomodels, Facultat de Ciències de la Terra, Universitat de Barcelona, Carrer Martí i Franquès s/n, 08028 Barcelona, Spain

[4] Département Géosciences et Environnement, CY Cergy Paris Université, Cergy-Pontoise, France

[5]Università degli Studi di Roma Tre, Dipartimento di Scienze, Sezione di Scienze Geologiche, Largo San Leonardo Murialdo 1, 00146 Rome, Italy

**Corresponding author: andrea.schito@ub.edu*

Keywords

South China Sea northern margin; rifted margin thermal evolution; vitrinite reflectance; biomarkers; thermal modelling

Abstract

The evolution of the rifted margin of the northern South China Sea challenges predictions of previous models but a knowledge gap still exists regarding how thermal history varies at different locations and times of rifting. International Ocean Discovery Program (IODP) Expeditions 367/368/368X collected samples of sediment that can be used to model the thermal evolution at different rifting stages in the distal margin and oceanic crust. Modelling results outline a thermal history driven by the interplay of different tectonic processes that are sometimes at odds with the main theoretical models. The most proximal location has a burial history that includes the unroofing of ~3km of sediment before the increase of heat flow during rifting and break up prior to cooling to the present day. In the more distal part, short, localised peaks in heat flow due to syn-rift magmatism are recorded while, the oceanic crust has a thermal regime decoupled from that of the continental section and here the rate of cooling abruptly decreased in final post-rift phases. Thus, while the transect drilled in IODP 367/368 may represent a transition from continental to ocean crust, the thermal regimens sampled by are not end-members in a simple continuum and instead capture fundamental steps in the thermal evolution of the distal rifted margin of the northern South China Sea. On a global scale, this dataset represents one of the most complete samplings of a distal rifted margin providing critical new constrains on the thermal evolution during formation of rifted margins.

1. ***Introduction***

The thermal structure of rifted margins controls the rheological behaviour of continental lithosphere during continental break-up (Buck, 1991; Manatschal et al., 2006; Geoffroy et al., 2015; Pérez-Gussinyé et al., 2024) as well as the stratigraphic architecture and sedimentation (Pindell et al. 2014; Alves et al. 2020). Thermal evolution of sedimentary basins fostered an extensive scientific interest in the 1970s because of its implication in hydrocarbon generation (Sleep, 1971) that is, today, still critical for evaluating the potential to host resources for the energy transition (Pérez-Gussinyé et al., 2023).

The classical Mckenzie model on stretched continental crust was developed in 1978 and considers an initial increase in heat flow (HF), culminating in a peak, followed by an exponential decline, with both phases strongly controlled by the degree of stretching (i.e. β factor; McKenzie, 1978). By contrast, the variation of oceanic crust depth and heat flow with age has been later constrained by Stein and Stein (1992) by compiling globally collected present- day HF values.

However, the variation of thermal structure in space and over time for a rifted margin remains largely unaddressed. There is most uncertainty about the evolution of distal rifted margins characterized by extreme lithospheric thinning, polyphase tectonic and localized magmatic activity; e.g. cases where variation is likely to be greatest. These domains remain poorly constrained mostly due to the lack of extensive offshore drilling along present-day distal rifted margins. Where outcrops exist the thermal history of initial sedimentary burial has been generally "overprinted" by metamorphism during orogenic events that inverted the rifted margin and lifted it to the surface (Beltrando et al., 2014). Only in specific cases, the thermal evolution of distal rifted margins imbricated within orogenic systems is still preserved (Alps: Beltrando et al., 2015; Celini et al., 2023; Pyrenees: Lescoutre et al., 2019; Saspiturry et al., 2020).

The only available studies of present-day distal rifted margins are based on 1) ODP and IODP expeditions such as the Iberia-Newfoundland rifted margins (Callies et al., 2018) and the South China Sea (Nirrengarten et al., 2020a) and/or 2) geophysical surveys such as the Iberia-Newfoundland rifted margins (Welford et al., 2010), Red Sea (Girdler and Evans, 1977), Gulf of Aden (Lucazeau et al., 2008), Guaymas Basin (Neumann et al., 2023), and the South China Sea (Zhu and Liu, 2025).

Studies and campaigns on present-day distal rifted margins suggest that geological features such as polyphased rifting, sedimentation rate, localized magmatism or ridge jumps can affect the syn-rift and post-rift thermal evolution (e.g. Neumann et al., 2023; Lucazeau et al., 2008). However, this has never been verified by means of thermal maturity studies except for one location corresponding to the Continental Ocean Transition (COT) of the South China Sea by Nirrengarten et al. (2020a).

Similarly, Lescoutre et al. (2019) and Saspiturry et al. (2020), in the fossil Iberian margin preserved in the Pyrenean orogen, have compared the maximum temperatures reached at different rifting stages calculated by numerical modelling with those qualitatively derived from reflectance and Raman analyses on the organic matter. Noteworthy, in these works, a kinetics-based calibration could not be applied because of very high thermal maturity, equating to or exceeding the onset of metamorphism.

Amongst the cases available, the South China Sea (SCS) has a unique dataset combining IODP Expeditions 367-368 -368X that sampled different crustal domains from the continental crust to the oceanic domain with pre, syn and post rift sediments obtained (Larsen et al. 2018), geophysical surveys and extensive seismic data (Gao et al., 2015; Lei et al. 2019; Ding et al., 2018; Deng et al., 2020) enabling us to investigate the thermal evolution of a rifted margins in space from continental crust to the oceanic crust and time across the rifting stages.

Results from these expeditions revealed a rapid lithospheric extension leading to sharp transition between continental crust and oceanic crust with no mantle exhumation (Larsen et al., 2018; Mohn et al., 2022; Zhang et al., 2024), along with localized magmatic activity during both rifting (Nirrengarten et al., 2020a; Deng et al., 2020; Zhang et al., 2021) and post-rift phases (Lin et al., 2019; Sun et al., 2019; Hung et al., 2021; Li et al., 2022; Sun et al., 2023) and a “rift-jump” at 27 Ma and 23 Ma toward the present-day spreading centre (Barckhausen et al., 2014; Ding et al. 2018).

The present-day thermal state of the whole Northern margin of the SCS has also been studied by a recent review (Zhu and Liu, 2025) outlining a general continent to the ocean HF increase with several exceptions recognized due to changing tectonic settings and shallow environmental factors that thus needs more investigation.

Here we present thermal histories for pre, syn- and post-rift sediments found at the distal rifted margin (U1501), the COT (U1499, U1502) and the oceanic domain (U1500) of the South China Sea, calibrated by organic proxies and relative kinetic models. Therefore, the full temperature time evolution of the northern rifted margin of the SCS is assessed at different locations and successive stages of rifted margin development, not only peak temperatures, presenting a unique dataset as a valuable reference for comparison with other rifted margins across the world.

2. Geological setting

The South China Sea (SCS) is a marginal oceanic basin located in the western Pacific and surrounded by continental units: the South China Block to the North, Indochina to the West and Palawan-Borneo to the South-East and the Luzon Arc to the East (Fig. 1a). It can be divided into three main sub basins (North West, East and South West, Fig. 1a) whose genesis relates to rift evolution. The tip of the V-shaped oceanic basin points to the south-east indicating a propagation of seafloor spreading that separated the northern China-Indochina margin from the Palawan-Borneo Block between ~33 Ma and ~15 Ma (Taylor and Hayes, 1983; Briais et al., 1993). The rifting of the SCS initiated in a former Mesozoic active continental margin that was generated by the subduction of the Paleo-Pacific plate under SE Eurasia (Zhou et al., 2008) during the Jurassic and Early Cretaceous (Li et al., 2020). Extension was suggest to have started in the late Cretaceous, based on evidence of development of extensional basins and non-marine sediments in the Pearl River Mouth Basin (Fig. 1a; Ru and Pigott, 1986; Zhou et al., 1995). The main episode of rifting occurred in Northern rifted margin and its conjugate margin located offshore Palawan, during late Eocene – early Oligocene that lead to breakup and seafloor spreading of the NE sub-basin (Larsen et al., 2018). Different hypotheses have been made on the cause of the rifting including: 1) roll-back of the subduction zone (Li et al., 2020);

2) slab-pull of a subducted proto South China Sea (Taylor and Hayes, 1983) or; 3) the collision between the Indian subcontinent and Asia (Tapponnier et al., 1990).

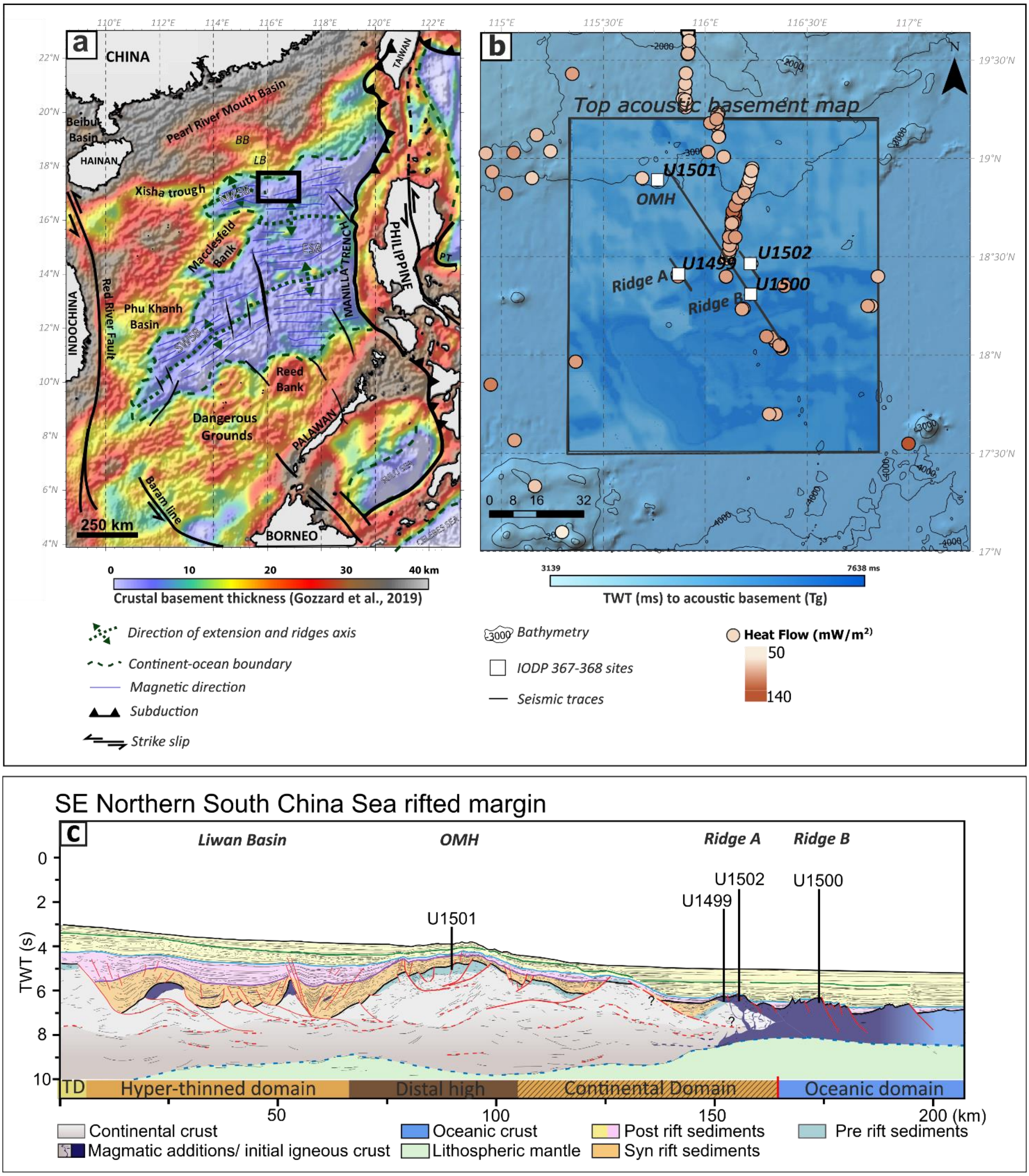

Figure 1 a) Crustal thickness map of the South China Sea modified from Legeay et al. 2024). Location of the study area (in black) in the Northern margin. Acronyms: BB: Baiyun Basin; LB – Liwan Basin; NWSB – North West South Basin; ESB – East Sub Basin; SWSB – South West Sub Basin. b) Spot of the study area from Fig. 1a. In the rectangle the map of the top acoustic basement (Tg reflector; Larsen et al., 2018) has been superimposed on the bathymetric map by using similar colour (see legend for Tg depths). The location *of the four studied IODP sites is indicated by the white dots. Heat flow location and values from Zhu and Liu, 2025 are indicated with the pale to dark brown dots. c) Seismic section with location of Site U1501, U1502, U1499 and U1500. The black line indicates the Tg unconformity (see text below) while the dotted line the Moho's depth.*

The analysis of thermal regime we present here is based on samples from four (U1499, U1500, U1501 U1502) of the seven sites drilled by the IODP expeditions 367-368 and 368X (Fig. 1b) across a ~90 km long section of the distal northern rifted margin (Fig. 1b and c) (Larsen et al., 2018): the Outer Margin High (OHM), the COT and the oceanic crust that span over three margin-parallel basement ridges, namely ridge A, B and C (Fig. 1b – sites C was not included in this work).
The OMH, sampled by site U1501, is a top basement high ~50 km wide composed of 15 to 20 km thick continental crust that progressively thins oceanward (Fig. 1c; Sun et al., 2018) and separates the Liwan sedimentary basin (LW, Fig. 1a) with a highly thinned continental crust to the north from the distal rifted margin to the south (Fig. 1c). Ridge A is a faulted structural high which has a variable top basement lithology: highly altered Mid-Ocean Ridge (MORB) basalts (U1502) and continental pre- to syn- rift clastic sediments (U1499). It represents the Continent-Ocean transition as it has characteristics of both continent and ocean basement (COT). By contrast, at Ridge B, a 7 km thick landward-rotated fault block, the sampled basement recorded MORB basalts with pillow structures (U1500, Fig. 1c) at the location of the C11n magnetic anomaly, interpreted as the first formed oceanic crust (Larsen et al., 2018).

2.1 Stratigraphy

Using biostratigraphic and lithostratgraphic data from the four holes, combined with geodynamic events of the SCS (Sun et al., 2018), the sedimentary sequences is divided into four main depositional units (Fig. 2): late-post Rift (Neogene), early-post Rift (late Oligocene), syn-rift (Early Oligocene to Eocene) and pre-rift (pre-late Eocene).

A more detailed stratigraphic information and lithologies are provided in Schito et al. (2026).

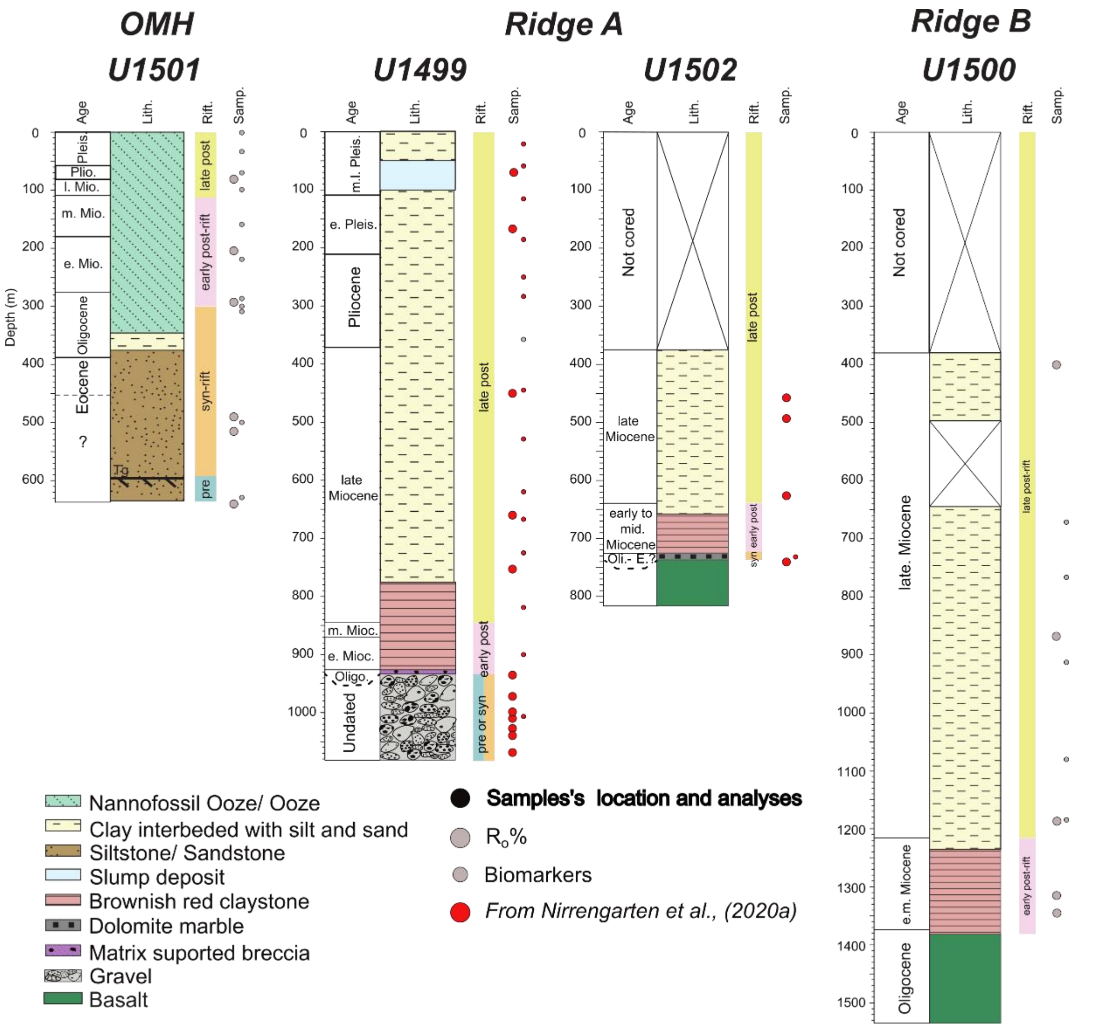

Figure 2 Stratigraphy and lithology of the four sites across the northern rifted margin of the SCS. Big-grey dots indicate location of samples analysed for vitrinite reflectance; small-grey dots indicate samples analysed with GC-MS. Red dots indicate samples analysed in Nirrengarten et al., (2020a)

2.1.1 Outer Margin High (OMH)

Site U1501 was investigated by four holes, our samples come from holes U1501C and U1501D (Tables 1). The Neogene sequence is composed by 290 m thick clay-rich nannofossil ooze and nannofossil ooze deposited in a deep-marine environment. The contact between the Neogene and Oligocene sediments is characterized by a major unconformity (T60) dated at 24-28 Ma by Jian et al. (2018), and Late Oligocene early post-rift and Early Oligocene to Eocene syn-rift successions are more than 300 m thick and consist of variable amounts of clay, silt, and sand (Fig. 2). In the syn-rift successions the oldest most reliable age control at the Eocene/Oligocene suggests the sandstones are the base are Eocene in age. Below an unconformity at 598.91m, well-lithified sandstones with unknown age represent the pre-rift succession.

2.1.2 *Ridge A*

At site U1499, the 929m thick Neogene Unit composed of clay, silt and sandstones and upper Oligocene–upper Miocene reddish-brown claystone was sampled to characterize the post-rift maturity, while undated gravels and breccias collected from the base of the boreholes represent the syn-post rift stage (Fig. 2).

At site U1502 the few samples collected derive from the late-post-rift late Miocene clay interbedded with silt and sands and from a thin layer of saddle dolomite that has been dated at the late Eocene age suggesting deposition during a late syn-rift setting (Fig. 2).

2.1.3 *Ridge B*

Site U1500 the post-rift succession was samples from 400 to 1200m of depth and is composed by late Miocene clay, silt and sands and by and early middle Miocene early-post-rift red clays (Fig. 2). The base of the borehole is composed by 150m of unaltered Oligocene (MOR) basalts (Fig. 2).

3 Methods

3.1 Thermal maturity and modelling calibration

Organic proxies' kinetics are the most used in burial/thermal modelling at low diagenetic levels. Vitrinite reflectance (R_o%) and Hopane 22S and Sterane 20S were used to calibrate our models. Sample's preparation and measurements for both organic petrography and biomarkers analyses are described in Schito et al. (2026) including R_o% histograms.

Simplified reconstructions of burial and thermal histories of drilling sites from the SCS were performed by using Basin Mod 2-D, a commercial software package for basin modelling. The main assumptions made during modelling are that: (1) rock decompaction is constrained following Sclater and Christie's method (1980), by fitting models to porosity data measured by the the standard IODP procedure (Moisture and Density – MAD; Sun et al., 2018 and supplementary material); (2) variations in seawater depth were modelled according to biostratigraphic data from Jian et al. (2018), and surface temperatures (ST) and sediment water interface temperatures (SWIFT) were taken from present-day measurements and corrected for paleo-latitudes; (3) thermal modelling was performed using the Easy %Ro method based on Sweeney and Burnham (1990), while hopane and sterane isomerisation was modelled according to the kinetic models proposed in Mackenzie and McKenzie (1983); (4) heat flow during rifting was modelled according to McKenzie et al., (1978).

4 Results

4.1 Organic Thermal maturity

Additional details regarding the dataset are provided in Schito et al. (2026).

4.1.1 Outer Margin High – site U1501

Assessing the level of thermal maturity of the post-rift to syn-rift Oligocene to Pliocene oozes from site U1501 is difficult because of a low organic carbon content that makes organic petrography impractical (TOC 0.40 -0.53 %), along with the shallow depth of burial (Tab. 1, Fig. 3 and Schito et al., 2026) and overall low level of thermal maturity as described later. The presence of hopane biomarkers with 17β,21β (H) structure conformations is important as these biomarkers are only stable at very low levels of diagenetic alteration (Farrimond et al, 1998). The values observed for a thermal maturity parameter based on these 17β,21β (H) hopanes for the Oligocene to Pliocene sediments of U1501 is consistent with the shallow depth of burial even if it does not describe a downhole trend. Conversely, most samples from the U1501-Oligocene to Pliocene oozes values for the hopane 22S (0.35 to 0.65) and sterane 20S (0.3 to 0.6) thermal maturity parameters that are inconsistent with the depth of burial show the presence of 17β,21β (H) Hopanes (Table 1) and sterene (Sup. Materials and Schito et al., 2026). The high values of hopane 22S and sterane 20S in most samples reflect an allochthonous input of reworked biomarkers. One sample at 308 meters depth (Tab. 1, Fig. 3b) likely reflects in-situ maturity for this interval with both collaborating hopane 22S and sterane 20S values of 0.14 and 0.17, and values that are reasonable for the sample's depth of burial and proportion of 17β,21β (H) hopane. This provides the one calibration point that can be used for modelling the youngest section of U1501.

Table 1 Samples' names, relative depths and rift stages for site U1501 together with TOC, Ro% values with standard deviation and number of measurements and Hopane 22S, ββ Hopane and Sterane 20S parameters. Hopane thermal maturity parameters calculated from the m/z 191 ion chromatogram include: C_{31} hopane 22S = C_{31} 17α,21β(H)-22S / [C_{31} 17α,21β(H)-22S + C_{31} 17α,21β(H)-22R]; C_{30} hopane ββ = C_{30} 17β,21β(H) / [C_{30} 17β,21β(H) + C_{30} 17β,21α(H) + C_{30} 17α,21β(H)]. Sterane thermal maturity parameters calculated from the m/z 217 ion chromatogram include: C_{29} sterane 20S = C_{29} 5α,14α,17α(H)-20S / [C_{29} 5α,14α,17α(H)-20S + C_{29} 5α,14α,17α(H)-20R].

Name	Depth (mbsf)	Rift stage	TOC (%)	Ro (%)	sd	n° of meas.	Hopane C_{31}22S	Hopane C_{30}ββ	Sterane C_{29}20S
U1501									
U1501C-1H-1W	0.05	Late Post-Rift	-	-	-	-	0.51	0.05	0.41
U1501C-4H-6W	35.85	Late Post-Rift	-	-	-	-	0.52	0.32	0.35
U1501C-8H-6W	73.69	Late Post-Rift		-	-	-	0.53	0.15	0.36
U1501C - 9H 5W	81.9	Late Post-Rift	0.4	-	-	-	-		-
U1501C-11H-5W	100.84	Late Post-Rift		-	-	-	0.65	0.09	0.32
U1501C-18F-4W	160.8	Early Post-Rift		-	-	-	0.64	0.04	0.56
U1501C - 28F 1W	204.76	Early Post-Rift	0.43	-	-	-	-		-

U1501C-31F-3W	220.87	Early Post-Rift		-	-	-	0.44	0.21	0.35
U1501C-43X-5W	289.35	Early Post-Rift		-	-	-	0.5	0.27	0.36
U1501C - 43X 5W	290.24	Early Post-Rift	0.53	-	-	-	-		-
U1501C-44X-5W	298.99	Early Post-Rift					0.43	0.21	0.41
U1501C-45X-5W	308.56	Early Post-rift		-	-	-	0.14	0.44	0.17
U1501D - 8R 1W	491.36	Syn-rift	1.31	0.38	0.05	53	-		-
U1501D-9R-1W	500.85	Syn-rift		-	-	-	0.58	0.12	0.32
U1501D - 11R CC	519.75	Syn-rift	5.14	0.35	0.05	86	-		-
U1501D - 26R 1W	634.82	Pre-rift	0.11	0.52	0.05	10	0.47	0.13	0.43

Vitrinite reflectance values range between 0.35 to 0.38 R_o% in the Eocene Syn-rift succession located above the reflector Tg. The succession from U1501 has high TOCs from 1.31 to 5.14 % (except for the deepest sample 0.11 %; Table 1). Under reflected light observation, the organic matter can be seen to be mostly vitrinite, likely indicating a significant input of terrestrial sedimentary organic matter. Biomarker data show some anomalous values in the Eocene of U1501 (Fig. 3 a and b), thus the highest vitrinite value of 0.38 R_o% may be influenced by the allochthonous and reworked organic matter.

Beneath the acoustic basement of U1501, in pre- late Eocene pre-rift succession, there is a jump in thermal maturity with an observed vitrinite reflectance of 0.52 R_o% (Tab. 1, Fig. 3a) that is further confirm by consistent increases in hopane and sterane thermal maturity parameters (Tab. 1, Fig. 3b).

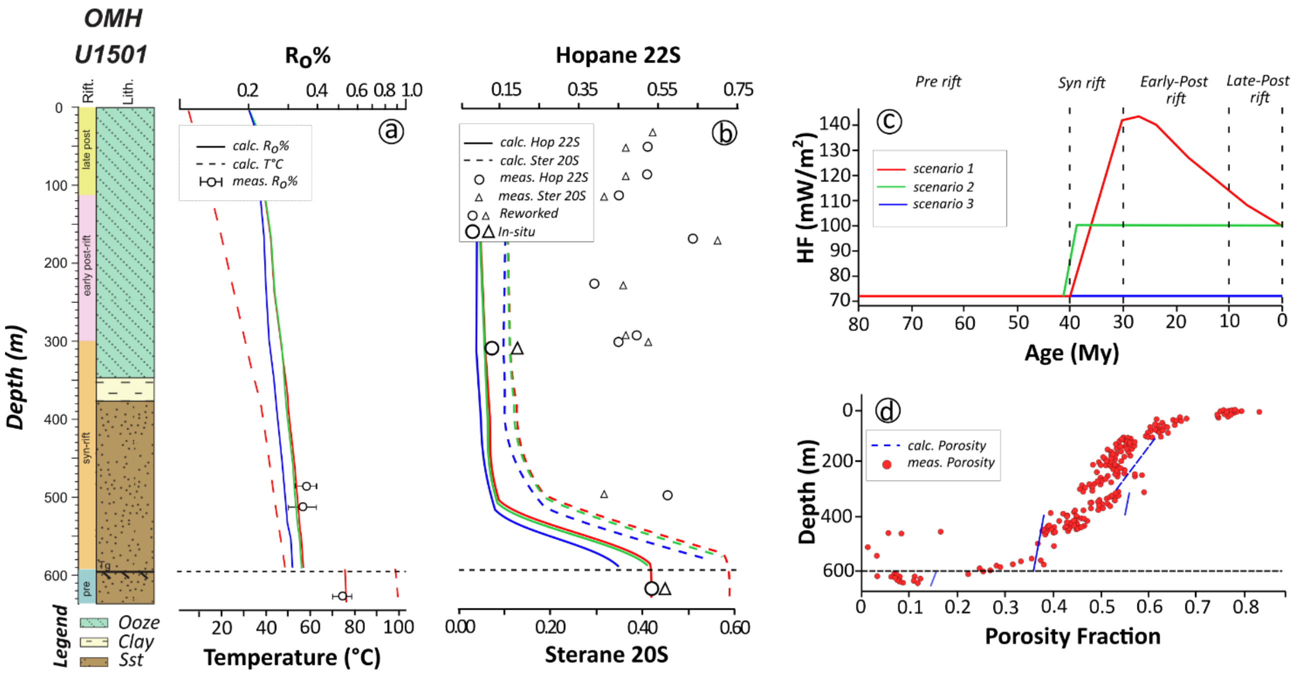

Figure 3 a) thermal model calibration of vitrinite data and resulting maximum temperatures; b) thermal model calibration of hopane and sterane data; c) The figure shows the three scenarios used to fit post-rift data. Scenario 1: Mckenzie's heat flow model for rifted margin using a beta factor of 2; Scenario 2; constant heat flow to present day values in the syn and post rift stages and 70 mW/m^2 in the pre-rift stage; Scenario 3: constant HF value of 70 mW/m^2; d) porosity data and calibrated curves. Sst in the stratigraphic legend stands for sandstones.

4.1.2 Ridge A – Sites U1499 and U1502

Results of the analyses of samples from ridge A were presented in Nirrengarten et al. (2020a) with the addition of a GC-MS analysis from site U1499 at 357m depth (Fig. 2 and Table S1 in sup. materials).

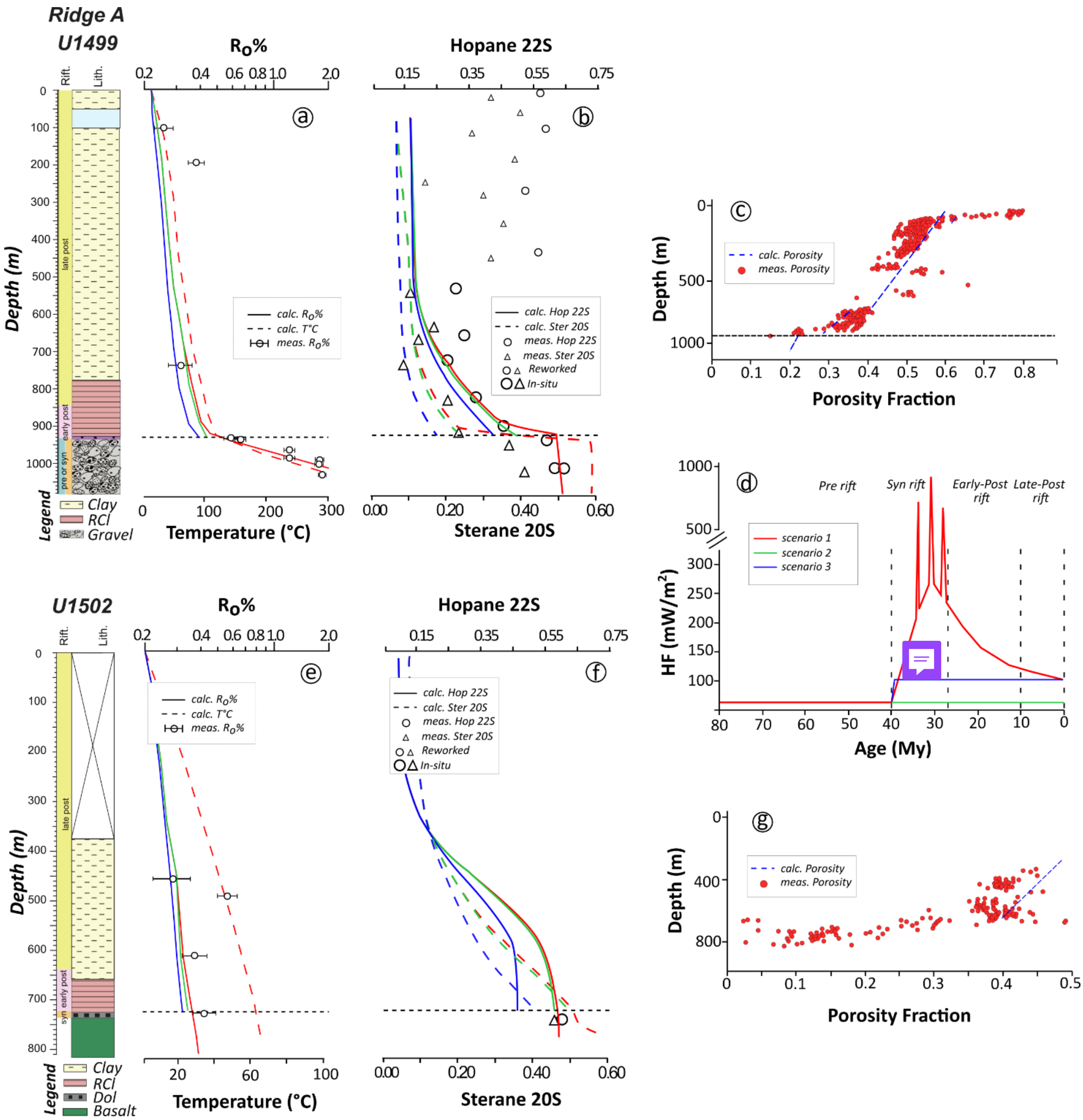

Figure 4 a) R_o% calibration and calculated maximum temperatures of U1499 well; b) Hopane 22S and Sterane 20S calibration model, of U1499 well; c) measured and calculated porosity evolution with depths, of U1499 well; d) The figure shows the three scenarios used to fit po-rift data. Scenario 1: heat flow evolution at the ocean-continent transition according to Mckenzie heat flow model for rifted margin using a beta factor of 4 and considering results from Nirrengarten et al., (2020a); Scenario 2; constant heat flow to present day values in the syn and post rift stages and 70 mW/m² in the pre-rift stage; Scenario 3: constant HF value of 70 mW/m²; e) Ro% calibration and calculated maximum temperatures of U1502 well; f) hopane 22S and sterane 20S calibration model, of U1502 well; g) measured and calculated porosity evolution with depths, of U1502 well. RCl in the stratigraphic legend stands for red claystones, while Dol for dolomite.

Late-post rift shales and mudstones deposited during the early to middle Miocene at site U1502 and up to the late Pleistocene in U1499 have R_o% values between 0.26 and 0.57 (Tab. S1). TOC is also relatively high at 0.3 to 1.3 % reflecting good quality organic matter for petrographic analyses. Despite this, the two highest values of vitrinite reflectance (0.41 and 0.57 R_o%) may reflect the presence of reworked material. This is validated by biomarker thermal maturity parameters that highlight a predominance of allochthonous material at the shallowest depths of site U1499 (Fig. 4), while the lowest values at the base of late-post Rift sediments confirm the low maturity detected by vitrinite reflectance (Fig. 4 b and Tab. S1 sup. materials).

Biomarker hopane and sterane thermal maturity parameters (Table S1) also confirm low maturity in the early-post Rift sediments in both sites, where TOC values suggest insufficient organic matter for reliable R_o% measurements. Syn and pre-rift sediments, on the other hand, show an exponential increase of vitrinite reflectance values in borehole U1499 reaching a maximum value of 1.83 R_o% at the bottom of the well (Fig. 4a), while a vitrinite reflectance of 0.43 R_o% for the hydrothermally altered dolomite in U1502 is high for the depth of burial, but perhaps not excessively high considering the implied metasomatism (Tab. S1 and Fig. 4e).

4.1.3 Ridge B – Site U1500

TOC data from the Oligocene claystones at about 1300 m of depth show TOC values between 0.59 and 0.66 and Ro value of 0.31 and 0.33% (Tab. 2), indicating an immature stage of hydrocarbon generation. Low maturities are further confirmed by Sterane and Hopane data in the Late Post Rift samples between 913 and 1185m of depth while the shallowest samples between 671 and 767m of depth indicate the presence of reworked material (Tab. 2 and Fig. 5).

Table 2 Samples' names, relative depths and rift stages for site U1500 together with TOC, Ro% values with standard deviation and number of measurements and Hopane 22S, ββ Hopane and Sterane 20S parameters. Hopane thermal maturity parameters calculated *from the m/z 191 ion chromatogram include: C_{31} hopane 22S = C_{31} 17α,21β(H)-22S / [C_{31} 17α,21β(H)-22S + C_{31} 17α,21β(H)-22R]; C_{30} hopane ββ = C_{30} 17β,21β(H) / [C_{30} 17β,21β(H) + C_{30} 17β,21α(H) + C_{30} 17α,21β(H)]. Sterane thermal maturity parameters calculated from the m/z 217 ion chromatogram include: C_{29} sterane 20S = C_{29} 5α,14α,17α(H)-20S / [C_{29} 5α,14α,17α(H)-20S + C_{29} 5α,14α,17α(H)-20R].*

Name	Depth (mbsf)	Rift stage	TOC (%)	Ro (%)	sd	n° of meas.	Hopane C_{31}22S	Hopane $C_{30}\beta\beta$	Sterane C_{29}20S
U1500									
U1500A - 4R 2W	400.48	Late Post-Rift	0.35	-	-	-	-	-	-
U1500A-18R-2W	671.86	Late Post-Rift		-	-	-	0.24	0.41	0.14
U1500A-28R-1W	767.46	Late Post-Rift		-	-	-	0.37	0.28	0.37
U1500B - 4R 1W	865.72	Late Post-Rift	0.26	-	-	-	-	-	-
U1500B-9R-1W	913.74	Late Post-Rift		-	-	-	0.19	0.5	0.12
U1500B-26R-2W	1080.2	Late Post-Rift		-	-	-	0.15	0.42	0.14
U1500B-37R-1W	1185.3	Late Post-Rift		-	-	-	0.36	0.36	0.27
U1500B - 50R 1W	1311.2	Late Post-Rift	0.66	0.31	0.1	10	-	-	-
U1500B - 53R 3W	1342.8	Late Post-Rift	0.59	0.33	0.1	14	-	-	-

4.2 Thermal modelling

Thermal histories were obtained for the OMH, Ridge A and Ridge B by evaluating which of three basal HF-models (scenarios graphically illustrated in Figs. 3c,4d,5c) best recreates measurements of vitrinite reflectance or the hopane 22s and sterane 20S thermal maturity parameters. These thermal maturity parameters have kinetic models (models that explain the parameter as a function of both heating duration and a given temperature) and thus may help in evaluating heat flow during past stages of rift development. The match between measured and model-calculated petrophysical parameters such as bulk density and thermal conductivity is also presented in tables and figures and tables from S2 to S5 in the supplementary materials.

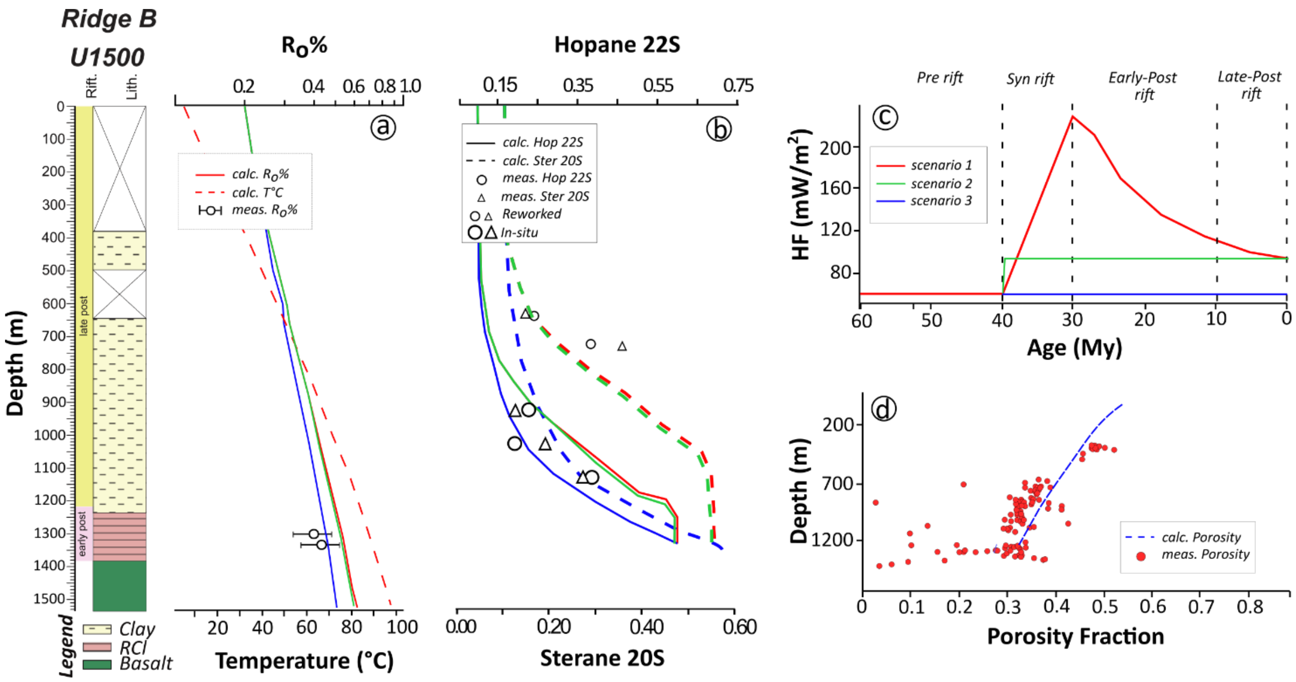

Figure 5 a) Ro% calibration and calculated maximum temperatures of U1500 well; b) Hopane 22s and Sterane 20s thermal maturity profiles; c) The figure shows the three scenarios used to fit po-rift data. Scenario 1: heat flow evolution at the ocean-continent transition according to Mckenzie heat flow model for rifted margin using a beta factor of 4; Scenario 2; constant heat flow to present day values in the syn and post rift stages and 70 mW/m2 in the pre-rift stage; Scenario 3: constant HF value of 70 mW/m2; d) measured and calculated porosity versus depth. RCl in the stratigraphic legend stands for red claystones.

Scenario 1) presents the situation where HF is high during rifting but subsequently subsides according to the McKenzie et al., (1978) model and can be considered a model that reflects both crustal and deep earth processes in the form of its beta-factor; Scenario 2) has a heat flow that is low in the pre-rift (70 mW/m^2) that is an average value for an active continental margin for Allen and Allen (2013; see discussion below) and then elevated for syn- and post-rift stages up to the present day, and; Scenario 3) represents the simplest and most facile consideration of heat flow by assuming that it has not changed over time (70 mW/m^2).

Based on the present-day thickness of the crust (15km) at the OMH a beta factor of 2 was chosen (Nirrengarten et al., 2020a,b). It was found that measurements of thermal maturity could be recreated for syn- and post-rift successions by heat flow models constructed using Scenarios 1 and 2 (Fig. 3 a, b, c). A rise in heat flow is needed, but the low number of observations makes further differentiation difficult. A model in which a maximum heat flow of 140 mW/m^2 is reached during the climax of rifting at 30 My before cooling to the present-day value of 100 mW/m^2, was found to still recreate thermal maturity, and this places a limit on the maximum heat flow subsequent to the onset of rifting (Fig. 3c). For the acoustic basement (section beneath the Tg horizon) and the pre-Eocene sediments, no rifting-based models of heat flow (Models after Scenario 1 that use beta factors) could recreate the high thermal maturity indicated by both vitrinite reflectance and biomarker data (i.e. there is jump in thermal maturity). Porosity is also much lower in the pre-Eocene sediments, and in combination with thermal maturity and seismic observations (Larsen et al. 2018) indicates the presence of an erosive unconformity. Adding 3 km of sedimentary burial and erosion before the onset of rifting, created a basin model that reproduced measurements of both porosity and thermal maturity. Thus, a lost burial history and particularly the erosion of overburden play an important role in the thermal history at the OMH, while basal heat flows can be explained by a more classical model of rifting (McKenzie, 1978).

For Ridge A (sites U1499 and U1502) previous work show a crustal thickness of 10 km suggesting an extreme thinning associated with a beta factor of >3 (Nirrengarten et al. 2020a). In post-rift sediments, heat flow models after Scenarios 1 and 2 (cooling subsequent to rifting or a steady at 110 mW/m^2) were equally able to recreate thermal maturity measurements. However, for site U1499 additional heat flow was needed for deeper units, and Nirrengarten et al., (2020a) invoked the emplacement of a magmatic intrusion, at least 20 m thick, near to the site. The thermal aureole around the intrusion must have started during the late syn-rift stage at the end of the Eocene and lasted to the beginning of the Oligocene and did not affect post rift successions.

Ridge B, (site U1500), the most distal site with post-rift sediments deposited on ocean crust, has low values of thermal maturity that cannot be predicted by heat flow models from Scenario 1 or 2, that reflect the effects of heating subsequent to rifting of continental crust. Measurements of thermal maturity at Ridge B were predicated by a constant heat flow of 70 mW/m^2 (Fig. 5).

5. Discussion

5.1. A combined approach for shallow sedimentary successions

Core samples from the IODP 367/368 offer the opportunity to model, for the first time, the evolution of heat flow in a rifted margin across a continent-to-ocean transect.

In the relatively shallow successions of the SCS this is achieved by combining organic proxies sensitive to early diagenetic transformation. The use of vitrinite reflectance is often limited by the lack of vitrinite in non-clastic sediments or sediments at very low stages of thermal maturation (i.e. pre-vitrinite), thus combining biomarker and vitrinite proxies was crucial to provide a continuous thermal maturity profile along the OHM and Ridge A (Figs. 3 and 4), and to confirm thermal maturity when only a few vitrinite reflectance measurements are made, such as beneath the Tg reflector in U1501 or the sparse samples in U1500 and U1502. Furthermore, the presence of sterene and 17β,21β (H) Hopanes (Schito et al., 2026), that are easily destroyed at high temperatures, suggest, in shallow samples, that a high percentage of reworked material is present avoiding misinterpretation during models' calibration (Wen et al., 2026).

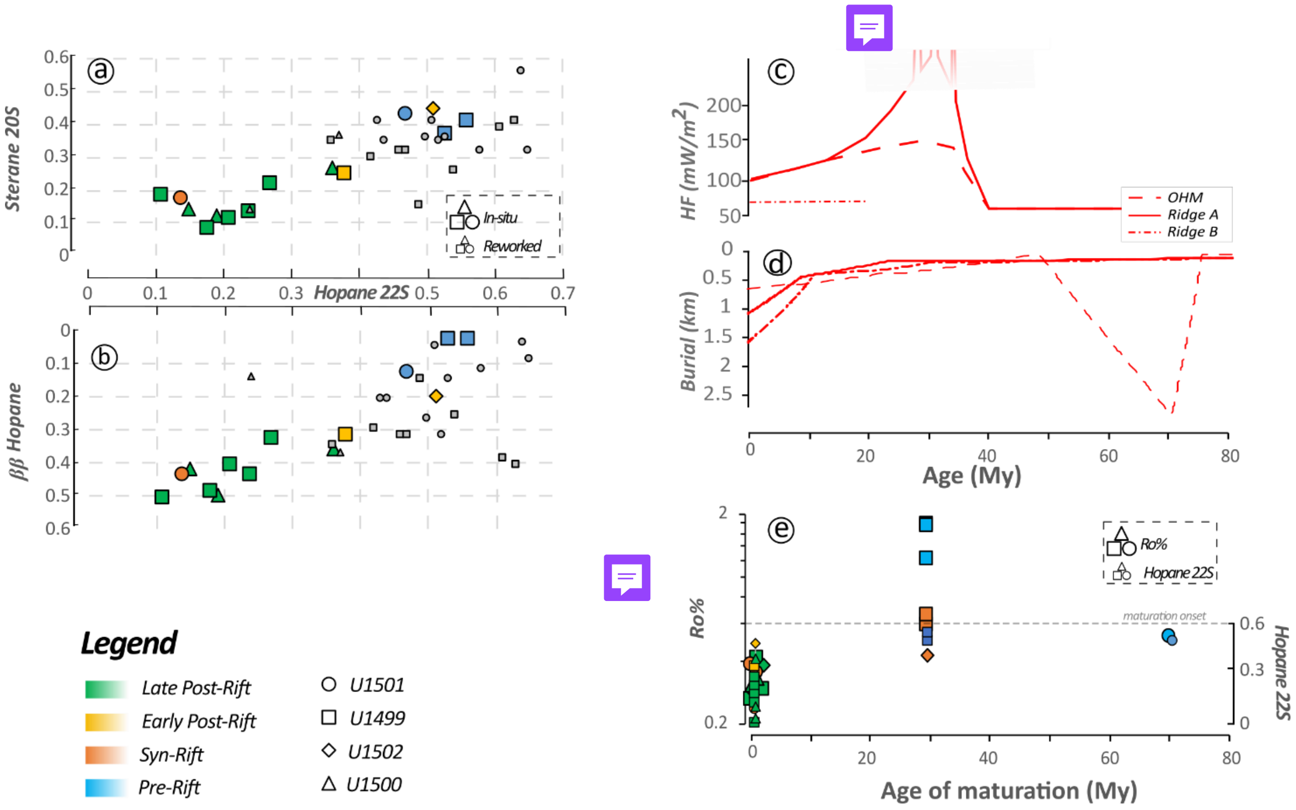

Figure 6 a) Sterane 20S and b) ββ hopane data plotted against Hopane 22s (note here the inverse order of the y-axis). c) heat flow and d) burial histories used to model thermal maturity data. Sea-level variation has not been included in this graph but is has been used in modelling calibration. e) thermal maturity expressed as R_o% and Hopane 22S against the age of maturation used in modelling. R_o% in logarithmic scale. Note that reworked data has not been used in figure e.

However, determining thermal maturity from a single biomarker proxy is not advisable and consistency among different proxies should be checked (Aderoju and Bend, 2017). This can be shown in Fig. 6 a and b where Hopane 22S has been plotted against Sterane 20S (Fig. 6a) and ββ hopane (17β,21β (H) Hopanes; Fig. 6b). Samples interpreted as exhibiting consistent changes in thermal maturity and thus can be taken as recording in-situ thermal alteration (big symbols). Reworked data (smaller symbols), mainly cluster in both upper right corners that correspond to the highest maturities.

Considering in-situ data alone, Figs. 6 a and b depict an increase in thermal maturity progressing from Pre-Rift to Late Post Rift samples. Late post-rift samples show the lowest level of thermal maturity and are associated with the shallowest depths at Ridge A and the OMH, and with depths beneath 1000m at Ridge B (U1500).

The calibration of models with vitrinite reflectance and biomarkers data allows increases in heat flow across the OHM and Ridge A at 30 My (Fig. 6 c) during the main phases of burial to be determined: one increase in just the OHM, at the end of Mesozoic before rifting of the SCS (dotted line in Fig. 6 d) and another, related to the increase in sedimentation rate from the last 10 My up to the present day in ridges A and B (solid and dash dotted lines in Fig. 6 d). Such phases, give us the timing of maturation of our samples as shown in Fig. 6 e, where for simplicity all thermal maturity data have been converted into R_o% equivalent according to models' results. The causes of differences in the timing of maturation across the rifted margin reflects geodynamic events specific to each site that have occurred since the end of Mesozoic and are discussed below.

5.2. Thermal evolution of the northern rifted margin of the SCS

5.2.1. OMH – A Mesozoic history recorded by pre-rift successions

Models of thermal evolution at the OMH (Fig. 3c) require that from 30 Ma HF decreased from a peak at the time of breakup, or that HF was maintained constant at a similar value to the present day. Prior to the Eocene and mostly likely prior to Cenozoic rifting, based on thermal maturity and porosity considerations, the OMH was buried under a 3km thickness of sediment and thus has a lost portion of its burial history. That needs further consideration.

Pre-rift successions comprise well-lithified and poorly sorted arkose with a high plagioclase content ranging from 30 to > 60 % that were likely derived from diorite or granodiorite or basement of intermediate composition. The age of the unit is not constrained because of the lack of fossils. However, across the Pearl River Mouth Basin (Fig. 1), the Tg horizon that marks acoustic basement is usually a boundary between Eocene and Mesozoic sediments, representing a hiatus thought to have lasted from Late Cretaceous to Paleogene (Yan et al., 2014). During the late Mesozoic, in the OMH, was an active continental margin, forming above a Paleo-Pacific subduction zone (Fig. 7a; Li et al., 2019; Xu et al., 2016). Sediments deposited at this time derived from the products of a Mesozoic Andean-type volcanic arc located to the front of present day coastal Southern China (Fan et al., 2022) and the Pre-rift sandstone, have a mineral composition that is near to intermediate (low in ultramafics and relatively low in quartz) largely consistent with this tectonic setting.

Both porosity and multiple thermal maturity parameters place strong limits for minimum burial for the sediments beneath Tg at U1501 (Fig. 3d). It is important to note that a burial of not less than 3 km is indicated, and a deeper burial might be possible if sediments accumulated in a basin with a low heath flow (Fig. 3 a,b,d). Within 1D basin modelling both tectonic burial (burial due to over-thrusting) and burial beneath sediments need to be considered. Considering a tectonic burial is it known that regionally a late Mesozoic compression led to the development of nappe stack (Ye et al., 2018) but only a gentle folding has been observed in some seismic sections in the basement of the OMH (Larsen et al. 2018). As well, folds and thrust faults below the Tg in the Baiyun-Liwan Sag exists (Zhao et al., 2020). Therefore, a tectonic loading due to thrusting and equivalent to >3 km of burial is still possible but difficult to demonstrate within currently known tectonic frameworks for the site. Conversely, burial beneath a thickness of 3 km of sediment in a forearc setting (Fig. 7a), as demonstrated for similar settings, is a more conservative explanation (Gusmeo et al., 2022). Regardless of the type of burial the pre-rift thermal history of the OMH requires the removal of 3 km of sediment.

The first event that may be responsible for removal of sediment prior to the Eocene is the development of the Eurasian active continental margin and its associated uplift and erosion of sediments (Fig. 7b; Shi and Li, 2012). This would have occurred prior to the onset of rifting during the Mesozoic and early Cenozoic in the SCS. The second event is associated with the formation of the adjacent Liwan basin (a sub-basin of the PRMB) to the north, that lead to rift flank uplift of the OMH during Cenozoic rifting (Lei et al. 2019). Lei et al (2019) suggested an age for this uplift of Late

Eocene-early Oligocene based on the absence of the the Enping Formation (32-38 My) in a nearby well drilled in the Liwan basin. However, the poor dating of the oldest pre-rift sandstones in borehole U1501, does not exclude an earlier age for the uplift or unroofing in part or whole and given the amount of sediments removed it is more probable most of the erosion was linked to the pre-Eocene regional uplift (Fig. 7b).

5.2.2. Ridge A – Syn-rift magmatic emplacement at the COT

Thermal evolution of Ridge A is already detailed in Nirrengarten et al. (2020a), who interpreted the high thermal maturities of syn- to pre-rift sediments to be a consequence of localised aureoles generated by magma emplacement during the continental break-up. Late and early post rift sediments have thermal maturities that can be explained by a paleo HF just above or equal to that of the present day (Fig. 4). Thus, in difference to the OMH, thermal evolution at the Ridge A is dominated by magmatism associated with break-up that produced locally heating and cooling at a shorter timescale than that of the entire crust (Fig. 7c).

Similarly to the OMH, the magmatism (at least at shallow levels) stopped after rifting and the thermal evolution at Ridge A during the burial of post-rift sediments corresponded to a cooling from peak heat flows (Scenario 1) or continuation of present-day values (Scenario 2; Fig. 4).

5.2.3. Ridge B – Thermal evolution on the oceanic crust

Thermal Evolution at Ridge B does not correspond to a McKenzie (1978) styled model of rifting of continental crust, nor to the Stein and Stein (1992) model for oceanic domain, nor can it be explained by a steady state model. However, complicating the assessment of thermal evolution at

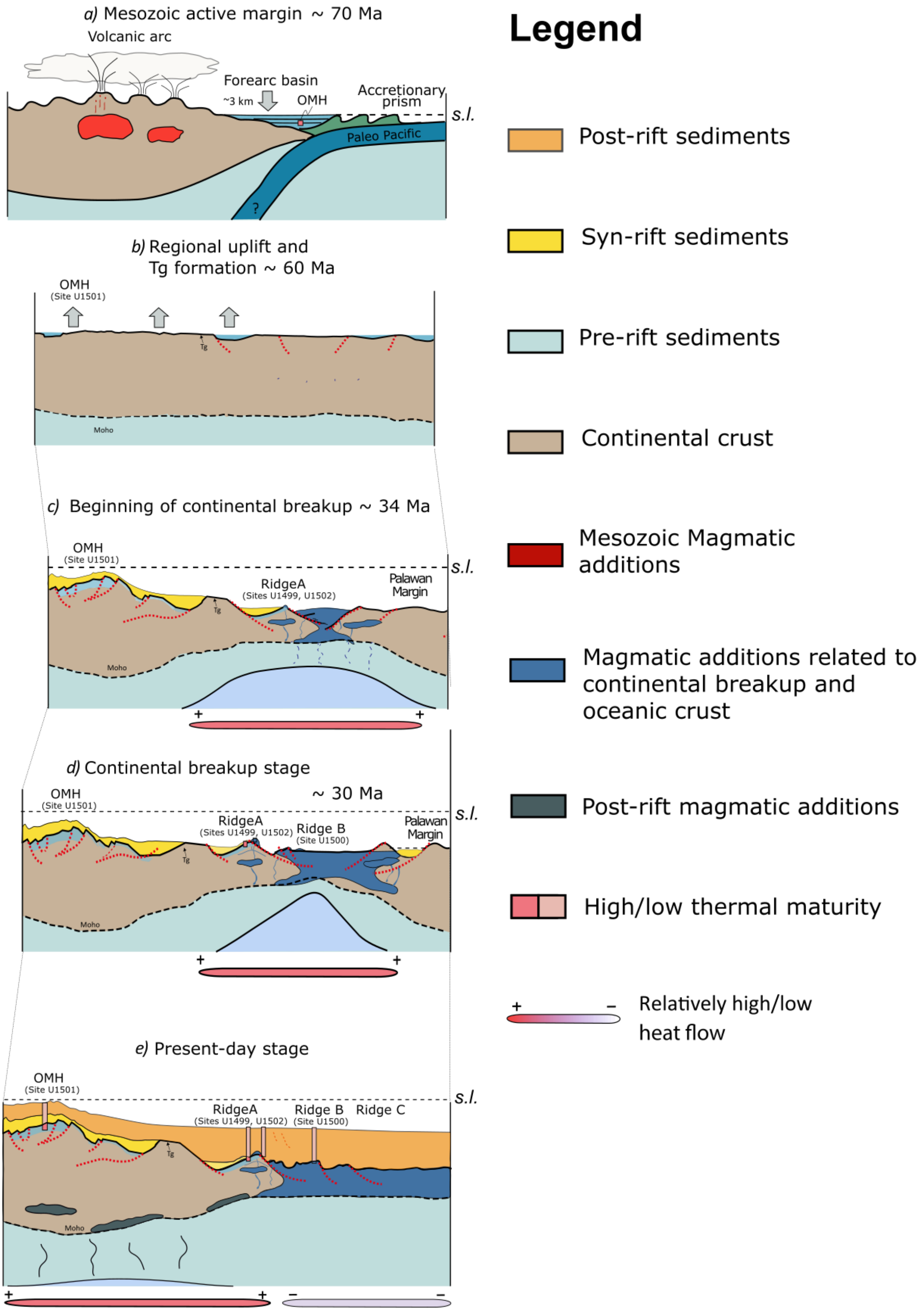

Figure 7 Tectonic evolution of the Northern rifted margin of the SCS according to outcomes from thermal models showing a) the Late Cretaceous active margin stage, b) condition at the onset of the Cenozoic rifting, c), d) development of the Cenozoic rifting and continental breakup, e) present-day stage.

U1500, Ridge B, is the use of a HF extrapolated from older sites (Nissen et al., 1995) or by comparison with the nearby U1499 site (Sun et al., 2018), as well as the generally low thermal maturity of the late post-rift succession.

According to our data, a HF value of at least 70 mW/m^2 since the early Oligocene (Fig. 5) could recreate thermal maturity in the post rift sediments even if, considering the age of the oceanic crust (30 Myrs old) and the proximity to Sites U1499 and U1502 a higher HF close to 100mW/m^2 should be expected.

However, oceanic spreading in this region is interpreted to have been associated with migration of the spreading centre during the formation of first igneous crust (Nirrengarten et al., 2020b) Asymmetric migration of spreading centre may have triggered slow-moving asthenospheric mantle material southward of ridge B during the establishment of stable seafloor spreading, leading to cooler conditions. In addition, the Ridge jump during 27Ma to 23 Ma (Barckhausen et al., 2014; Ding et al., 2018) may have further cooled the ridge B (Fig. 7 d and e). The causes of the Ridge jump are still not fully understood, but it has been proposed to be related to a far-field stress effect, induced by the adjacent Palawan-Borneo orogenesis linked to the subduction and closure of the Proto-South China Sea (Chang et al., 2022). As result, the thermal evolution of Ridge B and present-day low HF are related to the dynamics of seafloor spreading and it could be also speculated that the rapid cooling of the crust enhanced the thermal subsidence at Ridge B.

5.3. The distal rifted margin of the Northern SCS in a global framework of rifted margins

The thermal evolution of the distal rifted margin of the northern SCS described above differs in some ways from models previously proposed, but shares similarities with similar settings worldwide.

By using proxies of thermal maturity for which kinetics models are available it was possible for the first time to determine HF at different stages of rifting at different locations along the continent to ocean transect. Previous works determined thermal evolution at an extremely thinned continental crust mainly based on numerical modelling of HF values that were at most validated only by qualitative comparisons to vitrinite reflectance and Raman data (Lescoutre et al., 2019; Saspiturry et al., 2020). Direct measurements of heat flow are only available for basins where spreading is still ongoing at the present-day at basins like the Gulf of Aden and the Guaymas basin, or where recently active as in the SCS (Lucazeu et al., 2008; Neumann et al., 2019; Zhu and Liu, 2025).

Comparison with other approaches are not so straightforward since is not easy to find cross sections similar to ours, but despite this some synergy is observed. A good comparator can be made to Lescoutre et al. (2019) that document the transition along the Pyrenean rift, while Pérez-Gussinyé et al. (2024) model a full margin from continent to spreading ridge by varying sedimentation rates. Balázs et al. (2023) also model the Côte d'Ivoire margin, providing a reference for proximal settings. Present-day post-rift heat-flow data for rifted margins and continent–ocean transitions (COT) come from Lucazeu et al. (2008) in the Gulf of Aden, with complementary oceanic-crust values from Lucazeu et al. (2008) and Neumann et al. (2023) in the Guaymas Basin. Zhu and Liu (2025) provide additional heat-flow observations from the northern South China Sea, showing similarly high heat flow at the COT and lower values toward the oceanic crust.

These data are summarized in Fig. 8 where the red line indicates our calculated HF histories, the orange polygons indicate the ranges of HF values at each stage from the abovementioned works and the shaded green and red rectangles the present-day data from the Gulf of Aden, Guaymas basin and SCS.

As a first assumption to interpret the figure, it is worth nothing that we consider only the shape of the HF histories independently of the duration of the rifting. In practice it means the skewness of the curve is normalized based on a common duration, which is divided into the three main stage of rifting (Fig. 4).

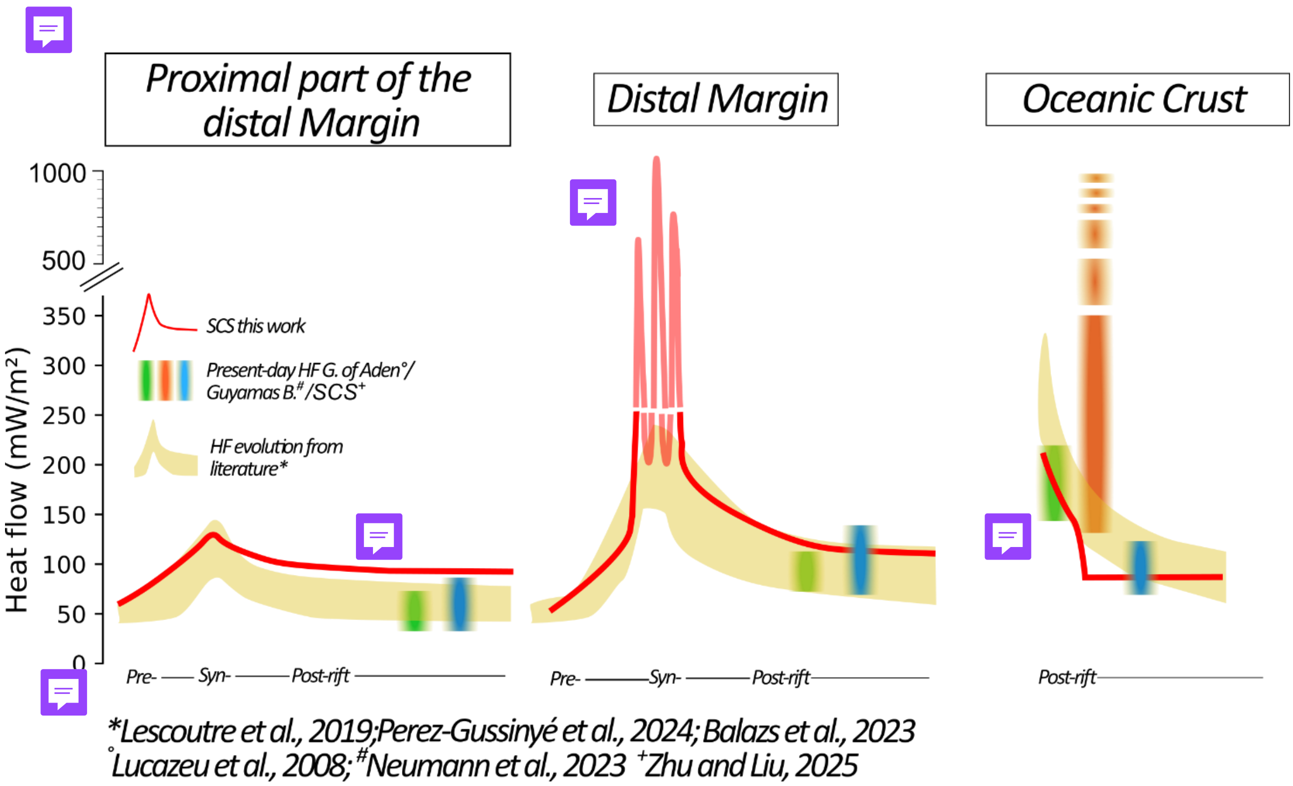

Figure 8 Comparison between the SCS thermal history calculated in this work and those from other studied margins and present-day data.

At the proximal margin, the pre-rift evolution is driven by relatively shallow subsidence probably in a forearc setting, with sediment derived by the erosion of a magmatic arc. This active margin setting is directly followed by a late Mesozoic and early Cenozoic post-orogenic extensional event and the Cenozoic rifting likely without thermal equilibration in-between.

This is substantially different from other rifted margins like the North Atlantic, the Tethys or the Red-Sea/Gulf of Aden where a thickened crust after continental collision (i.e. Variscan or Pan-African orogens respectively) was present and reequilibrated before the start of the subsequent rifting.

In the SCS, the lithosphere was probably in high thermal conditions and weakened by the large amount of water released by the subduction of the Pacific (Nirrengarten et al. 2020b; Wang et al., 2019).

As shown in Fig. 8 the SCS evolution follows the general trend calculated in previous works, even if towards the highest values. Here the maximum values do not exceed the 140 mW/m^2 (more or less the peak calculated in our models). It has to be considered that no real constraint exists on these values since the heat generated was not enough to overcome the heating produced by the Mesozoic burial. However, this is a maximum estimation, since higher values would have overcome the temperatures of about 80-100º C reached during pre-rift burial.

In contrast, the thermal evolution of the distal margin, including the hyper-thinned continental crust and the COT appears much more variable. In the early Cretaceous fossil Pyrenean rift, characterized by hyper-thinned continental crust, the maximum heat flow (HF) can reach up to 300 mW/m^2 then decreasing to approximatively 100 to 70 mW/m^2 at present day, as calculated by Lescoutre et al. (2019).

At the COT, the highest values reached in other basins are ~200 mW/m^2 at the breakup time according to the models by Perez-Gussinye et al. (2024) and the classical rift model (McKenzie, 1978). However, as shown in Nirrengarten et al. (2020a) in the SCS at the COT, HF increases can be locally higher at the time of breakup than predicated by models.

Locally these higher temperatures are present and driven by syn-rift magmatism in a similar way to the present-day in the Guaymas basin, where sills intrusions and associated hydrothermalism produce short-lived elevated anomalous HF, and then subsequent cooling which is more rapid than typical cooling of crust (Neumann et al., 2023). HF value can be kept up to the present-day as observed in the Gulf of Aden (green rectangle in Fig. 8) related to recent post-rift volcanism (Lucazeau et al. 2008).

The high HF at both OHM and Ridge A is likely related to the presence of deep-seated magmatic bodies recognized at the base of the crust in the Pearl River Mouth Basin, that have been linked by many authors (Lin et al., 2019; Sun et al., 2019; Hung et al., 2021; Li et al., 2022; Sun et al., 2023) to the post-rift magmatism in the area (Fig. 7 d).

In the ocean domain, the Gulf of Aden follows the Stein and Stein (1992) or Goutorbe (2010) models after the syn-rift peak (Lucazeu et al., 2008). The SCS however clearly deviates from this expected behaviour at Ridge B. Here, possibly because of lithosphere heterogeneities, crustal deformation has moved through time producing the so-called “Ridge Jumps” that stop both deformation and excess heating. Ridge-jumps are also known in the Woodlark basin in the Pacific (Goodliffe and Taylor, 2007) where, on the other hand, the effect on cooling has still not been verified. What we demonstrated for Ridge B at the northern margin of the SCS is a slowing in rate of maturation, following the ridge-jump at 23 My, ultimately producing values that are lower and comparable with those used to model the SCS.

What can be picked up from Fig. 8 is that, in literature a general increase of the HF is always depicted moving from the proximal to the distal margin related to continental lithosphere thinning. The northern rifted margin of the SCS doesn’t fit this pattern showing the highest localized HF at the COT during syn-rift stages, conserving positive thermal anomalies at the proximal margin and COT (probably due to deep-post and shallow-syn-rift magmatism respectively) and then a drop from the last 10 Ma in oceanic crust in response to ridge-jump.

6. Conclusion

This study investigates the distal rifted margin of the northern SCS using an integrated approach based on organic petrography and biomarkers, allowing us to unravel the thermal evolution of the sedimentary successions deposited during the pre-, syn- and post-rift stages.

Using the results of the IODP expeditions 367/368, we studied the thermal maturities at four sites across different structural domains (OMH; ridges A and B). These results were used to calibrate four thermal models.

The thermal evolution of the distal rifted margin of the SCS is characterized by a heterogeneous distribution of thermal maturity in pre-, syn-, and post-rift sediments, spanning from the continental to the oceanic domains. These variations in thermal maturity are linked to different tectonic events that shaped the formation of the SCS.

At Site U1501 (OMH), the preceding Mesozoic Yanshanian orogeny contributed to localized burial of pre-rift sediments, influencing their thermal maturity. During the syn-rift stage, extreme thinning of the continental lithosphere and high HF were dominant factors. Instead, thermal maturity in these sediments was likely influenced by localized events, such as magmatic intrusions and extrusions associated with rifting and continental breakup that had localized effects over shorter timescales.

The post-rift phase is generally characterized by a low thermal maturity trend, with localized anomalies and contrasts between the continental and oceanic sections. On the continental side, significant post-rift magmatic activity may have caused localized thermal anomalies in the sediments. In the oceanic domain, the instability of seafloor spreading resulted in complex mantle dynamics, driven by seafloor spreading migration and ridge-jumps.

These new results from the distal rifted margin of the northern SCS represent a unique dataset for global comparison with other rifted margins worldwide and provide key constraints on their thermal evolution.

Acknowledgements

The first author AS acknowledges the public fundings of the Ramón y Cajal Program (RYC-2022) nº RYC2022-036094-I MCIN/AEI/10.13039501100011033, funded by the Spanish Ministry of Science and Innovation and cofounded by the European Union (FSE+). This work used samples and data collected during International Ocean Discovery Program (IODP) Expedition 367/368/368X. We thank the participants of IODP Expedition 367-368 as well as the captains and crew of the *Joides Resolution*. AS thanks Platte River Associates for providing an academic licence of BasinMod 2D. GM acknowledges IODP France and ECORD for support. ZW gratefully acknowledges PhD studentship and support from the University of Aberdeen and the Chinese Scholarship Council (CSC). SAB gratefully acknowledges NERC award NE/R002576/1 and the technical support of Colin Taylor, University of Aberdeen.

The Royal Society of Edinburgh is also acknowledged for strengthening the collaboration between the University of Aberdeen and the University of Cergy-Pontoise through the RSE Saltire International Collaboration nº 1975 granted to AS.

References

Aderoju, T., & Bend, S., 2017. A comparative assessment of biomarker-based thermal maturity parameters. AAPG Memoir 114: Petroleum Systems Analysis—Case Studies. Pages 219-237 DOI: 10.1306/13602031M1143706

Allen, P. A., & Allen, J. R. , 2013. Basin analysis: Principles and application to petroleum play assessment. John Wiley & Sons, Oxford, UK

Alves, T., Fetter, M., Busby, C., Gontijo, R., Cunha, T.A., Mattos, N.H., 2020. A tectono-stratigraphic review of continental breakup on intraplate continental margins and its impact on resultant hydrocarbon systems. Mar. Pet. Geol. 117, 104341.

Balázs, A., Gerya, T., May, D., & Tari, G. 2023. Contrasting transform and passive margin subsidence history and heat flow evolution: Insights from 3D thermo-mechanical modelling. Geol. Soc. Spec. Publ. https://doi.org/10.1144/SP524-2021-94

Barckhausen, U., Engels, M., Franke, D., Ladage, S., Pubellier, M., 2014. Evolution of the South China Sea: Revised ages for breakup and seafloor spreading. Mar. Pet. Geol. 58, 599–611.

Beltrando, M., Compagnoni, R., Ferrando, S., Mohn, G., Frasca, G., Odasso, N., ... & Beltrando, M., 2014. Crustal thinning and mantle exhumation in the Levone area (Southern Canavese Zone, Western Alps). *A Field Guide Across the Margins of Alpine Tethys J. Virtual Explor., Electronic Edition*, *48*.

Beltrando, M., Stockli, D. F., Decarlis, A., & Manatschal, G., 2015. A crustal-scale view at rift localization along the fossil Adriatic margin of the Alpine Tethys preserved in NW Italy. *Tectonics*, *34*(9), 1927-1951.

Buck, W.R., 1991. Modes of continental lithospheric extension. J. Geophys. Res. Solid Earth 96, 20161–20178.

Callies, M., Filleaudeau, P. Y., Dubille, M., & Lorant, F., 2018. How to predict thermal stress in hyperextended margins: Application of a new lithospheric model on the Iberia margin. *AAPG Bulletin*, *102*(4), 563-585

Chang, S.-P., Pubellier, M., Delescluse, M., Qiu, Y., Nirrengarten, M., Mohn, G., Chamot-Rooke, N., Liang, Y., 2022. Crustal architecture and evolution of the southwestern South China Sea: Implications to continental breakup. Mar. Pet. Geol. 136, 105450.

Célini, N., Mouthereau, F., Lahfid, A., Gout, C., & Callot, J. P., 2023. Rift thermal inheritance in the SW Alps (France): insights from RSCM thermometry and 1D thermal numerical modelling. *Solid earth*, *14*(1), 1-16.

Deng, H., Ren, J., Pang, X., Rey, P.F., McClay, K.R., Watkinson, I.M., Zheng, J., Luo, P., 2020. South China Sea documents the transition from wide continental rift to continental break up. Nat. Commun. 11, 4583.

Ding, W., Sun, Z., Dadd, K., Fang, Y., Li, J., 2018. Structures within the oceanic crust of the central South China Sea basin and their implications for oceanic accretionary processes. Earth Planet. Sci. Lett. 488, 115–125.

Fan, C., Xia, S., Cao, J., Zhao, F., Wan, K., 2022. Seismic constraints on a remnant Mesozoic forearc basin in the northeastern South China Sea. Gondwana Res. 102, 77–94.

Farrimond, P., Taylor, A., TelnÆs, N., 1998. Biomarker maturity parameters: the role of generation and thermal degradation. Org. Geochem. 29, 1181–1197.

Gao, J., Wu, S., McIntosh, K., Mi, L., Yao, B., Chen, Z., & Jia, L., 2015. The continent–ocean transition at the mid-northern margin of the South China Sea. *Tectonophysics*, *654*, 1-19.

Girdler, R. W., & Evans, T. R. (1977). Red Sea heat flow. Geophys. J. Int., 51(1), 245-251.

Geoffroy, L., Burov, E.B., Werner, P., 2015. Volcanic passive margins: another way to break up continents. Sci. Rep. 5, 14828.

Goodliffe, A. M., & Taylor, B., 2007. The boundary between continental rifting and sea-floor spreading in the Woodlark Basin, Papua New Guinea. Geol. Soc. Spec. Publ., vo. 282, pp 217-238. Lyell collection, London.

Goutorbe, B., 2010. Combining seismically derived temperature with heat flow and bathymetry to constrain the thermal structure of oceanic lithosphere. *Earth Planet. Sci. Lett.*, *295*(3-4), 390-400.

Gusmeo, T., Schito, A., Corrado, S., Alania, V., Enukidze, O., Zattin, M., Pace, P., Cavazza, W., 2022. Tectono-thermal evolution of central Transcaucasia: Thermal modelling, seismic interpretation, and low-temperature thermochronology of the eastern Adjara-Trialeti and western Kura sedimentary basins (Georgia). J. Asian Earth Sci. 237, 105355.

Hung, T.D., Yang, T., Le, B.M., Yu, Y., Xue, M., Liu, B., Liu, C., Wang, J., Pan, M., Huong, P.T., 2021. Crustal structure across the extinct mid-ocean ridge in South China sea from OBS receiver functions: insights into the spreading rate and magma supply prior to the ridge cessation. Geophys. Res. Lett. 48, e2020GL089755.

Jian, Z., Larsen, H.C., Alvarez Zarikian, C.A., 2018. Expedition 368 preliminary report: South China Sea rifted margin. Prelim. Rep. 368.

Larsen, H.C., Mohn, G., Nirrengarten, M., Sun, Z., Stock, J., Jian, Z., Klaus, A., Alvarez-Zarikian, C.A., Boaga, J., Bowden, S.A., Briais, A., Chen, Y., Cukur, D., Dadd, K., Ding, W., Dorais, M., Ferré, E.C., Ferreira, F., Furusawa, A., Gewecke, A., Hinojosa, J., Höfig, T.W., Hsiung, K.H., Huang, B., Huang, E., Huang, X.L., Jiang, S., Jin, H., Johnson, B.G., Kurzawski, R.M., Lei, C., Li, B., Li, L., Li, Y., Lin, J., Liu, C., Liu, C., Liu, Z., Luna, A.J., Lupi, C., McCarthy, A., Ningthoujam, L., Osono, N., Peate, D.W., Persaud, P., Qiu, N., Robinson, C., Satolli, S., Sauermilch, I., Schindlbeck, J.C., Skinner, S., Straub, S., Su, X., Su, C., Tian, L., van der Zwan, F.M., Wan, S., Wu, H., Xiang, R., Yadav, R., Yi, L., Yu, P.S., Zhang, C., Zhang, J., Zhang, Y., Zhao, N., Zhong, G., Zhong, L., 2018. Rapid transition from continental breakup to igneous oceanic crust in the South China Sea. Nat. Geosci. 11, 782–789. https://doi.org/10.1038/s41561-018-0198-1

Legeay, E., Mohn, G., Ringenbach, J. C., Vetel, W., & Sapin, F., 2024. 3D structure of low-angle normal faults and tectono-sedimentary processes of nascent continental core-complexes in the SE South China Sea. *Tectonics*, *43*(8), e2023TC008218.

Lei, C., Alves, T.M., Ren, J., Pang, X., Yang, L., Liu, J., 2019. Depositional architecture and structural evolution of a region immediately inboard of the locus of continental breakup (Liwan Sub-basin, South China Sea). GSA Bull. 131, 1059–1074.

Lescoutre, R., Tugend, J., Brune, S., Masini, E., & Manatschal, G., 2019. Thermal evolution of asymmetric hyperextended magma-poor rift systems: Results from numerical modeling and Pyrenean field observations. *Geochem. Geophys. Geosyst.*, *20*(10), 4567-4587.

Li, F., Sun, Z., Yang, H., Lin, J., Stock, J.M., Zhao, Z., Xu, H., Sun, L., 2020. Continental interior and edge breakup at convergent margins induced by subduction direction reversal: A numerical modeling study applied to the South China Sea margin. Tectonics 39, e2020TC006409.

Li, G., Mei, L., Pang, X., Zheng, J., Ye, Q., Hao, S., 2022. Magmatism within the northern margin of the South China Sea during the post-rift stage: An overview, and new insights into the geodynamics. Earth-Science Rev. 225, 103917.

Lin, J., Xu, Y., Sun, Z., Zhou, Z., 2019. Mantle upwelling beneath the South China Sea and links to surrounding subduction systems. Natl. Sci. Rev. 6, 877–881.

Lucazeau, F., Leroy, S., Bonneville, A., Goutorbe, B., Rolandone, F., d'Acremont, E., Watermez, L., Düsünur, D., Tuchais, P., Huchon, P., Bellahsen, N., Al-Toubi, K., 2008. Persistent thermal activity at the Eastern Gulf of Aden after continental break-up. *Nat. Geoscience*, *1*(12), 854-858.

Mackenzie, A.S., McKenzie, D., 1983. Isomerization and aromatization of hydrocarbons in sedimentary basins formed by extension, Geological Magazine. https://doi.org/10.1017/S0016756800027461

McKenzie, D., 1978. Some remarks on the development of sedimentary basins. *Earth Planet. Sci. Lett.*, *40*(1), 25-32.

Manatschal, G., Engström, A., Desmurs, L., Schaltegger, U., Cosca, M., Müntener, O., Bernoulli, D., 2006. What is the tectono-metamorphic evolution of continental break-up: the example of the Tasna Ocean–Continent Transition. J. Struct. Geol. 28, 1849–1869.

Mohn, G., Ringenbach, J. C., Nirrengarten, M., Lei, C., McCarthy, A., & Tugend, J., 2022. Mode of continental breakup of marginal seas. *Geology*, *50*(10), 1208-1213.

Nirrengarten, M., Mohn, G., Schito, A., Corrado, S., Gutiérrez-García, L., Bowden, S.A., Despinois, F., 2020a. The thermal imprint of continental breakup during the formation of the South China Sea. Earth Planet. Sci. Lett. 531. https://doi.org/10.1016/j.epsl.2019.115972

Nirrengarten, Michael, Mohn, G., Kusznir, N.J., Sapin, F., Despinois, F., Pubellier, M., Chang, S.P., Larsen, H.C., Ringenbach, J.C., 2020b. Extension modes and breakup processes of the southeast China-Northwest Palawan conjugate rifted margins. Mar. Pet. Geol. 113, 104123.

Nissen, S.S., Hayes, D.E., Bochu, Y., Zeng, W., Chen, Y., Nu, X., 1995. Gravity, heat flow, and seismic constraints on the processes of crustal extension: Northern margin of the South China Sea. J. Geophys. Res. solid earth 100, 22447–22483.

Neumann, F.; Negrete-Aranda, R.; Harris, R. N.; Contreras, J.; Galerne, C. Y.; Peña-Salinas, M. S.; Spelz, R. M.; Teske, A.; Lizarralde, D.; Höfig, T. W.; Expedition 385 Scientists; Aiello, I. W.; Ash, J. L.; Bojanova, D. P.; Buatier, M.; Edgcomb, V. P.; Gontharet, S.; Heuer, V. B.; Jiang, S.; Kars, M. A. C.; Kim, J.–H.; Koornneef, L. M. T.; Marsaglia, K. M.; Meyer, N. R.; Morono, Y.; Pastor, L. C.; Pérez Cruz, L. L.; Ran, L.; Riboulleau, A.; Sarao, J. A.; Schubert, F.; Singh, S. K.; Stock, J. M.; Toffin, L. M. A. A.; Xie, W.; Yamanaka, T.; Zhuang, G., 2023. Heat flow and thermal regime in the Guaymas Basin, Gulf of California: Estimates of conductive and advective heat transport. *Basin Res.*, *35*(4), 1308-1328.

Pérez-Gussinyé, M., Collier, J. S., Armitage, J. J., Hopper, J. R., Sun, Z., & Ranero, C. R. 2023. Towards a process-based understanding of rifted continental margins. *Nature Reviews Earth & Environment*, *4*(3), 166-184.

Pérez-Gussinyé, M., Xin, Y., Cunha, T., Ram, R., Andrés-Martínez, M., Dong, D., García-Pintado, J., 2024. Synrift and post-rift thermal evolution of rifted margins: a re-evaluation of classic models of extension. Geol. Soc. London, Spec. Publ. 547, SP547-2023.

Pindell, J., Graham, R., Horn, B., 2014. Rapid outer marginal collapse at the rift to drift transition of passive margin evolution, with a Gulf of Mexico case study. Basin Res. 26, 701–725.

Ru, K., Pigott, J.D., 1986. Episodic rifting and subsidence in the South China Sea. Am. Assoc. Pet. Geol. Bull. 70, 1136–1155.

Saspiturry, N., Lahfid, A., Baudin, T., Guillou-Frottier, L., Razin, P., Issautier, B., ... & Corre, B., 2020. Paleogeothermal gradients across an inverted hyperextended rift system: Example of the Mauléon Fossil Rift (Western Pyrenees). *Tectonics*, *39*(10), e2020TC006206.

Schito, A., Mohn, G., Wen, Z., Corrado, S., Nirrengarten, M., Gutiérrez-García, L., Bowden, S., 2026. Thermal maturity data from the distal margin to the oceanic crust in the northern margin of the South China Sea. Data in Brief. Submitted

Sclater, J.G., Christie, P.A.F., 1980. Continental stretching: An explanation of the post-mid-Cretaceous subsidence of the central North Sea basin. J. Geophys. Res. Solid Earth 85, 3711–3739.

Shi, H., Li, C.-F., 2012. Mesozoic and early Cenozoic tectonic convergence-to-rifting transition prior to opening of the South China Sea. Int Geol Rev 54, 1801–1828.

Sleep, N. H., 1971. Thermal effects of the formation of Atlantic continental margins by continental break up. *Geophys. J. Int.*, *24*(4), 325-350.

Stein, C.A., Stein, S., 1992. A model for the global variation in oceanic depth and heat flow with lithospheric age. Nature 359, 123–129.

Sun, Q., Alves, T.M., Wu, S., Zhao, M., Xie, X., 2023. Early Miocene magmatism in the Baiyun Sag (South China Sea): A view to the origin of intense post-rift magmatism. Gondwana Res. 120, 127–144.

Sun, Z., Jian, Z., Stock, J.M., Larsen, H.-C., Klaus, A., Alvarez Zarikian, C.A., 2018. South China sea rifted margin. Proc. Int. Ocean Discov. Progr. 367.

Sun, Z., Lin, J., Qiu, N., Jian, Z., Wang, P., Pang, X., Zheng, J., Zhu, B., 2019. The role of magmatism in the thinning and breakup of the South China Sea continental margin: Special Topic: The South China Sea Ocean Drilling. Natl. Sci. Rev. 6, 871–876.

Sweeney, J.J., Burnham, A.K., 1990. Evaluation of a simple model of vitrinite reflectance based on chemical kinetics. Am. Assoc. Pet. Geol. Bull. 74, 1559–1570. https://doi.org/10.1306/0c9b251f-1710-11d7-8645000102c1865d

Tapponnier, P., Lacassin, R., Leloup, P.H., Schärer, U., Dalai, Z., Haiwei, W., Xiaohan, L., Shaocheng, J., Lianshang, Z., Jiayou, Z., 1990. The Ailao Shan/Red River metamorphic belt: tertiary left-lateral shear between Indochina and South China. Nature 343, 431–437.

Taylor, B, Hayes, DE, 1983. Origin and history of the South China Sea basin, in: Hayes, Dennis (Ed.), The Tectonic and Geologic Evolution of Southeast Asian Seas and Islands: Part 2. pp. 23–56.

Wang, P., Huang, C.-Y., Lin, J., Jian, Z., Sun, Z., Zhao, M., 2019. The South China Sea is not a mini-Atlantic: plate-edge rifting vs intra-plate rifting. Natl. Sci. Rev. 6, 902–913.

Welford, J. K., Smith, J. A., Hall, J., Deemer, S., Srivastava, S. P., & Sibuet, J. C., 2010. Structure and rifting evolution of the northern Newfoundland Basin from Erable multichannel seismic reflection profiles across the southeastern margin of Flemish Cap. Geophys. J. Int., 180(3), 976-998.

Xu, C., Shi, H., Barnes, C.G., Zhou, Z., 2016. Tracing a late Mesozoic magmatic arc along the Southeast Asian margin from the granitoids drilled from the northern South China Sea. Int. Geol. Rev. 58, 71–94.

Yan, P., Wang, L., Wang, Y., 2014. Late Mesozoic compressional folds in Dongsha Waters, the northern margin of the South China Sea. Tectonophysics 615, 213–223.

Ye, Q., Mei, L., Shi, H., Camanni, G., Shu, Y., Wu, J., Yu, L., Deng, P., Li, G., 2018. The Late Cretaceous tectonic evolution of the South China Sea area: An overview, and new perspectives from 3D seismic reflection data. Earth-Science Rev. 187, 186–204.

Welford, J. K., Smith, J. A., Hall, J., Deemer, S., Srivastava, S. P., & Sibuet, J. C. (2010). Structure and rifting evolution of the northern Newfoundland Basin from Erable multichannel seismic reflection profiles across the southeastern margin of Flemish Cap. *Geophys. J. Int.*, *180*(3), 976-998.

Wen, Z., & Bowden, S. A. (2026). The Submarine Transport of Reworked Petroleum from the Pearl River Mouth Basin to Distal Locations of the Northern South China Sea. Marine Geoscience and Energy Resources, 207682.

Zhang, C., Sun, Z., Manatschal, G., Pang, X., Li, S., Sauter, D., Péron-Pinvidic, G., Zhao, M., 2021. Ocean-continent transition architecture and breakup mechanism at the mid-northern South China Sea. Earth-Science Rev. 217, 103620.

Zhang, C., Manatschal, G., Taylor, B., Sun, Z., Zhao, M., & Zhang, J., 2024. Characterization and mapping of continental breakup and seafloor spreading initiation: The example of the northern rifted margin of the South China Sea. *Basin Res.*, *36*(4), e12882.

Zhao, F., Alves, T. M., Xia, S., Li, W., Wang, L., Mi, L., Wu, S., Cao, J., Fan, C., 2020. Along-strike segmentation of the South China Sea margin imposed by inherited pre-rift basement structures. *Earth Planet. Sci. Lett.*, *530*, 115862.

Zhou, D., Ru, K., Chen, H., 1995. Kinematics of Cenozoic extension on the South China Sea continental margin and its implications for the tectonic evolution of the region. Tectonophysics 251, 161–177. https://doi.org/10.1016/0040-1951(95)00018-6

Zhou, D., Sun, Z., Chen, H., Xu, H., Wang, W., Pang, X., Cai, D., Hu, D., 2008. Mesozoic paleogeography and tectonic evolution of South China Sea and adjacent areas in the context of Tethyan and Paleo-Pacific interconnections. Isl. Arc 17, 186–207.

Zhu, W., and Liu, S., 2025. Heat flow and thermal structure of the South China Sea. *Earth-Sci. Rev.*, *261*, 105028.

Declaration of interests

☒ The authors declare that they have no known competing financial interests or personal relationships

that could have appeared to influence the work reported in this paper.

☐ The authors declare the following financial interests/personal relationships which may be considered

as potential competing interests: